Hindawi
Advances in Civil Engineering
Volume 2021, Article ID 9916859, 15 pages
https://doi.org/10.1155/2021/9916859

Research Article

Accurate Virtual Trial Assembly Method of Prefabricated Steel Components Using Terrestrial Laser Scanning

Yin Zhou[1], **Daguang Han**[2], **Kaixin Hu**[3], **Guocheng Qin**[3], **Zhongfu Xiang**[1], **Chunli Ying**[3], **Lidu Zhao**[1] and **Xingyi Hu**[4]

[1]*Department of Civil Engineering, Chongqing Jiaotong University, Chongqing 400074, China*
[2]*Department of Building and Energy Technology, Oslo Metropolitan University, 0130 Oslo, Norway*
[3]*Chongqing Smart City and Sustainble Development Academy, Chongqing 400074, China*
[4]*Faculty of Engineering Technology, KU Leuven, 8000 Bruges, Belgium*

Correspondence should be addressed to Zhongfu Xiang; xzfywzy@163.com

Received 19 March 2021; Revised 17 May 2021; Accepted 3 June 2021; Published 16 June 2021

Academic Editor: Zhen Lei

The comprehensive utilization of prefabricated components (PCs) is one of the features of industrial construction. Trial assembly is imperative for PCs used in high-rise buildings and large bridges. Virtual trial assembly (VTA) is a preassembly process for PCs in a virtual environment that can avoid the time-consuming and economic challenges in physical trial assembly. In this study, a general framework for VTA that is performed between a point cloud, a building information model (BIM), and the finite element method is proposed. In obtaining point clouds via terrestrial laser scanning, the registration accuracy of point clouds is the key to building an accurate digital model of PCs. Accordingly, an accurate registration method based on triangular pyramid markers is proposed. This method can enable the general registration accuracy of point clouds to reach the submillimeter scale. Two algorithms for curved members and bolt holes are developed for PCs with bolt assembly to reconstruct a precise BIM that can be used directly in finite element analysis. Furthermore, an efficient simulation method for accurately predicting the elastic deformation and initial stress caused by forced assembly is proposed and verified. The proposed VTA method is verified on a reduced-scale steel pipe arch bridge. Experimental results show that the geometric prediction deviation of VTA is less than 1/1800 of the experimental bridge span, and the mean stress predicted via VTA is 90% of the measured mean stress. In general, this research may help improve the industrialization level of building construction.

1. Introduction

Large-scale building components are manufactured in factories in industrial construction. Assembly line production and a stable environment ensure that the prefabricated components (PCs) of a building exhibit reliability. The prefabricated construction method is widely used in large buildings and bridges. Compared with the on-site pouring method, the prefabricated assembly method demonstrates the advantages of fast construction and being environment friendly [1, 2]. However, the premise for a successful implementation of the prefabricated assembly method is that all PCs must be assembled accurately. When a manufacturing deviation of PCs causes an assembly failure or unacceptable effects, PCs must be returned to the factory for adjustment or remanufacturing. In many projects, the prefabrication factory is located far from the assembly site, and thus, rework or reconstruction will considerably increase project duration, cost, and risk. Therefore, conducting physical trial assembly (PTA) is necessary before transporting PCs to large-scale prefabricated assembly projects, although this process is not mandatory in accordance with the specifications. PTA can be considered actual assembly in advance in a factory. It requires equipment, workers, and site similar to field assembly; hence, it increases the cost and duration of a project. For large structures, such as bridges, PTA can only verify the assembly effect of adjacent segments due to site constraints. In addition, new dimension deviation

may occur during transportation, making the results of the physical trial assembly in the factory invalid. The use of digital models for virtual trial assembly (VTA) can avoid the problems experienced during PTA [3]. An accurate geometric dimension is a precondition of VTA for detecting geometric deviation. Previous studies used manual measurement to obtain the feature point coordinates of PCs [3]. However, with the development of photogrammetry technology, computer vision has been used to obtain more comprehensive geometric information [4–6]. Image calibration and distortion correction make the efficiency and reliability of the computer vision method insufficient. Terrestrial laser scanning (TLS) is a new technology for quickly and accurately capturing the 3D shape of physical objects. TLS is currently used in structure monitoring [7, 8], reverse modeling [9], and dimension inspection [10]. Considering the capability of TLS to acquire the 3D model of physical objects quickly, 3D scanning has been used to replace manual measurement when checking the assembly interface of PCs [10]. Further research has combined TLS and BIM technology for the dimension inspection and quality management of PCs, demonstrating progress from point cloud to BIM [11, 12]. However, the measurement error of a point cloud has not received sufficient attention in the reverse modeling process. A single scan can only obtain the point cloud of a part of the surface of a 3D component. To obtain the complete 3D digital model of a PC, the point clouds obtained by scanning in different directions around a PC must be registered. The geometric error of a point cloud typically has two parts: (1) the measurement error of a single point and (2) the registration error of multiple point clouds. The measurement error of a single point is a type of random noise. After implementing the point cloud noise reduction algorithm [13] and feature fitting (e.g., plane fitting and circle fitting), the single point measurement error can be significantly reduced [14]. Therefore, the registration error of a point cloud is the primary error source when measuring the size of PCs by using TLS. In VTA, the use of point clouds with registration errors may cause incorrect assembly results. For the forced assembly method that uses bolts or interference fit, small geometric deviations may cause force angular displacement that cannot be disregarded and may result in the redistribution of structural stress after assembly [15]. Therefore, the reduction of the registration error of a point cloud and assembly simulation that considers stress redistribution are two key points for the accurate prediction of engineering structures via VTA. This research contributes to the body of knowledge by providing a general methodological framework for VTA that uses TLS. In this framework, a registration method with submillimeter accuracy is proposed to eliminate the geometric errors of point clouds in the registration process and a virtual assembly method that combines reverse BIM and 3D finite element method (FEM) is developed to accurately predict the geometric shape and structural stress state of multiple PCs with manufacturing deviations after forced assembly.

In this paper, comparative experiments are first performed to verify whether the accuracy of the proposed point cloud registration method can meet the requirements of VTA. This condition is the prerequisite for accurate VTA that uses TLS. Then, the reverse modeling method of steel structure components and splicing parts is introduced from the point cloud by using a scaled arch bridge as an example. Furthermore, an experiment is conducted to verify whether the accuracy of the proposed simulation method has considered stress redistribution. Finally, the virtual assembly of the scaled arch bridge is realized in accordance with the proposed VTA framework. Physical assembly is simultaneously performed. The results of the physical and virtual assemblies are compared to prove the reliability of the proposed VTA method.

2. Related Work Background

2.1. Registration of Point Cloud. Point cloud registration can be divided into two methods: (1) real-time registration (2) and accurate registration of point cloud in different periods. Real-time registration refers to sensing the surrounding environment while scanning and then registering the real-time scanning point cloud with the acquired point cloud. Real-time registration is typically used in mobile laser scanning, and the widely adopted method is simultaneous localization and mapping [16–18]. Real-time registration is mostly used for fast modeling and indoor navigation; it is a low-precision point cloud registration method. For the accurate registration of different periods obtained using fixed scanners (such as TLS), the primary methods are registration based on markers [19, 20] and registration based on point cloud data [21, 22]. The common marker is the standard sphere, which has been widely used in terrestrial scanning systems. However, the reflection angle of the laser increases and the point coordinates are distorted near the edge of the sphere. This phenomenon is called edge drift. Therefore, problems in point cloud registration based on spherical markers still exist. The data-based registration method that has received widespread concern is the iterative closest point (ICP) method [21]. The principle of this method is to find the nearest point pair in two point clouds and use the distance matrix of the nearest point pair to estimate the rotation and translation parameters of the point cloud. However, if the overlap of point clouds is insufficient, then the success rate of the correct convergence of ICP is considerably reduced; that is, more scans are required in VTA. In addition, the distance function of ICP largely depends on the distance between points. In large scenes, excessively small point spacing will substantially increase the amount of point cloud data, increasing the scanning time and data processing cost. Therefore, ICP registration errors will accumulate during VTA in civil engineering, particularly for shape deviations caused by angle errors due to the large distance between points. Consequently, the registration error of point clouds is expected to be in submillimeter even in large structures. Although the ICP method has many variants [23, 24], most algorithms focus on efficiency, and thus, they cannot meet the submillimeter accuracy requirements of a VTA program.

2.2. Virtual Assembly. Building information models (BIMs) have been widely used in infrastructure construction in recent years [25–27]. BIMs are digital models of physical objects that can be used for visual display, rendering, progress simulation, and space inspection. Therefore, BIMs are used for the virtual assembly simulation of PCs [28]. Geometric parameters in BIMs are typically derived from design. Virtual assembly based on BIMs is limited to the rationality verification of the scheme, and it cannot be used in actual PC geometric detection and shape prediction. Recently, a large number of studies have focused on the reverse construction of BIMs from point clouds [29–32]. In accordance with the mode of model generation, reverse modeling can be divided into mesh encapsulation and feature extraction. Mesh encapsulation refers to the use of triangular meshes to connect adjacent points and form a space surface or shell. The accuracy of a mesh model is low due to the existence of point cloud noise, and the volume of data is not reduced. Thus, mesh models are unsuitable for VTA. Feature extraction refers to obtaining the feature parameters (e.g., centerline, corner, and radius) of physical objects by using the fitting algorithm in the point cloud and then reconstructing the BIM on the basis of the feature parameters [31]. At present, major research focuses on the calculation of section parameters and the axis extraction of typical components, such as walls, columns, and beams. Meanwhile, research on the assembly parts of PCs is less. Virtual assembly can be performed once a digital model acquires complete geometric information. Virtual assembly necessitates strictly using the geometric constraints of real components, such as face to face and center alignment. The result of an assembly with multiple constraints is not unique, and thus, a reasonable assembly pose must be determined. In the automobile and industry fields, many software programs use a tree diagram [33], which depicts the assembly relationship among different parts to evaluate the results of various assembly methods. Bolts are widely used in fabricated steel structures, and the generalized Procrustes analysis is adopted to determine the optimal posture for connections with multiple bolts [3]. Several recent studies have exerted effort to implement conventional VTA that uses TLS [34, 35]. The plane and line feature fitting algorithm is adopted to obtain the position coordinates of assembly points, and the least squares method is used to solve the optimal assembly parameters, which are only applicable to the rigid assembly process. For steel structures with multiple spliced ends, such as trusses, forced restraint will result in additional deformation that may be more significant than the shape deviation caused by manufacturing errors. When a PC is the primary load-bearing structure, forced restraint will generate additional stress and reduce structural safety. These conditions are not considered in the design. Therefore, solving the virtual assembly problem with stress redistribution for the structure to be loaded is essential.

3. Accurate Registration of Point Cloud

3.1. Triangular Pyramid Marker Design. The use of a marker is necessary because data-based registration methods are currently unable to achieve the submillimeter registration accuracy required by VTA. Although they are commonly used, spherical markers have disadvantages in VTA. The high accuracy of sphericity makes manufacturing and maintenance more demanding, and thus, registration spheres are frequently expensive. A registration sphere is typically small for portability and accuracy. The number of point clouds on a marker sphere is sparse in the scanning process of large steel structures. This situation leads to an increase in fitting error. Edge drift caused by an excessively large laser reflection angle inevitably occurs, as shown in Figure 1, due to the characteristics of the sphere. Edge drift is a nonuniform random noise because it is concentrated on the edge of the sphere. Thus, the calculation error of the spherical center coordinates cannot be disregarded. A new triangular pyramid marker is designed to overcome the shortcomings of a registration sphere, as shown in Figure 2. This triangular pyramid consists of detachable plates and brackets connected by universal ball hinges. Each plate can be adjusted at different angles in accordance with the scanning angle. This method solves the problem in which the reflection angle of the registration sphere is excessively large. In 3D space, three surfaces that are not parallel to one another can determine a unique coordinate system. Therefore, the accurate registration of a point cloud can be theoretically accomplished by using only one triangular pyramid marker.

3.2. Registration of a Triangular Pyramid Marker. During VTA, point clouds A and B, which have the same triangular pyramid markers, are obtained by scanning the same object from different scanning angles. Point cloud A is defined as the reference point cloud. Point cloud B is defined as the registered point cloud. After achieving accurate registration, point cloud B is converted into the coordinate system of point cloud A, and thus, it now coincides with point cloud A. First, the triangular pyramid point cloud is segmented in point clouds A and B. The plates of the triangular pyramid are separated from one another; hence, the point cloud of each plate is separated easily. The point cloud of each plate of the triangular pyramid is fitted via plane fitting. The next step is to make the fitting plane in point cloud B strictly overlap with the fitting plane in point cloud A. However, directly calculating rotation parameter R and translation parameter T converted from B to A on the basis of the characteristic parameters of the fitted plane is impossible due to random errors in plane fitting based on point clouds. The ICP algorithm estimates the best transformation parameters in two point clouds; this process is simple and easy. The ICP algorithm is widely used in commercial software. The primary steps of this algorithm are (1) sampling in point cloud A to obtain point set P, (2) finding the nearest point set Q of P in point cloud B, and (3) using the distance function between P and Q as the objective function. The objective function is minimized by iteratively calculating the optimal transformation parameters. Given that point clouds A and B are not exactly the same, no point set Q completely corresponds to point set P in point cloud B. Therefore, the ICP algorithm must have a registration error that depends on the

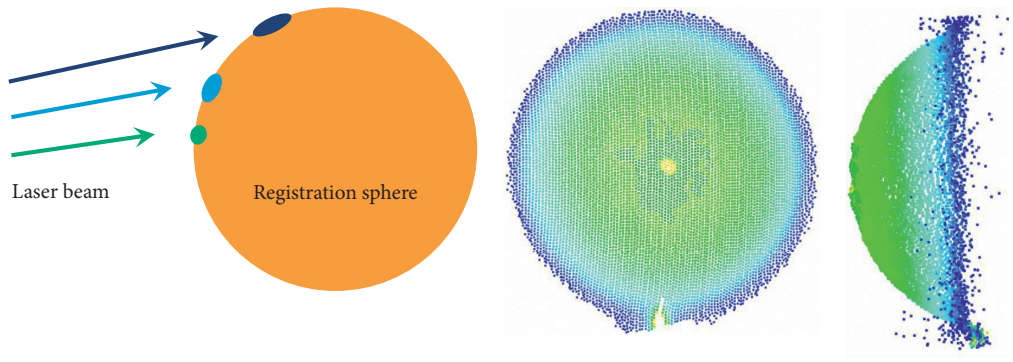

(a) (b) (c)

Figure 1: Edge drift of a spherical marker: (a) laser path of a registration sphere, (b) front view of a spherical point cloud, and (c) side view of a spherical point cloud.

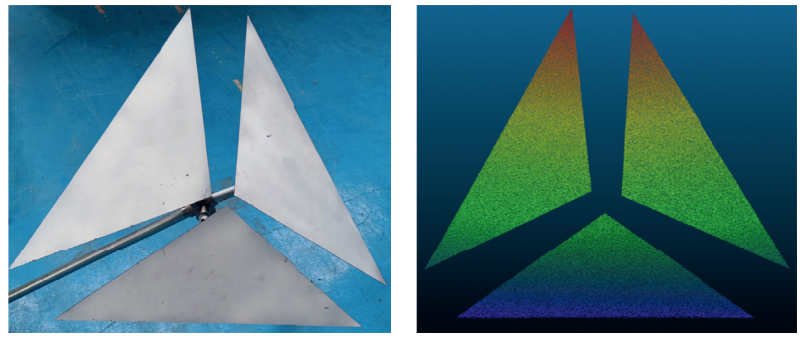

(a) (b)

Figure 2: Triangular pyramid marker: (a) physical picture of a triangular pyramid marker and (b) point cloud of a triangular pyramid marker.

density of a point cloud. The improved ICP algorithm is proposed for accurate registration of triangular pyramid markers. The complete process of using a triangular pyramid marker to register a point cloud accurately is illustrated in Figures 3 and 4. The method for generating point sets P and Q is depicted in Figure 3. In contrast with the ICP algorithm, set A is randomly generated on the fitting plane of a flat point cloud of point cloud A. The generation range is limited within the area of the plate. Then, point set A is projected onto the fitting plane of the flat point cloud of point cloud B to obtain point set Q. The detailed iterative process of calculating the transformation parameters is shown in Figure 4.

Suppose that the coordinate matrix of point set P is X_P. Then, the coordinate matrix of point set Q is X_Q. The conversion of Q into P can be calculated as follows:

$$X_P = RX_Q + T. \tag{1}$$

In formula (1),

$$R = \begin{bmatrix} \cos\beta\cos\gamma & \cos\beta\sin\gamma & -\sin\beta \\ -\cos a\sin\gamma - \sin a\sin\beta\cos\gamma & \cos a\cos\gamma + \sin a\sin\beta\sin\gamma & \sin a\cos\beta \\ \sin a\sin\gamma + \cos a\sin\beta\cos\gamma & -\sin a\cos\gamma - \cos a\sin\beta\sin\gamma & \cos a\cos\beta \end{bmatrix},$$
$$T = \begin{bmatrix} t_x, t_y, t_z \end{bmatrix}. \tag{2}$$

The symbols α, β, and γ are the rotation angles around the X-axis, Y-axis, and Z-axis, respectively. The symbols t_x, t_y, and t_z are the translation distances along the X-axis, Y-axis, and Z-axis, respectively. The singular value decomposition method is used to calculate the rotation matrix R and the translation vector T. First, the centroids C_P and C_Q of point sets P and Q are calculated using formula

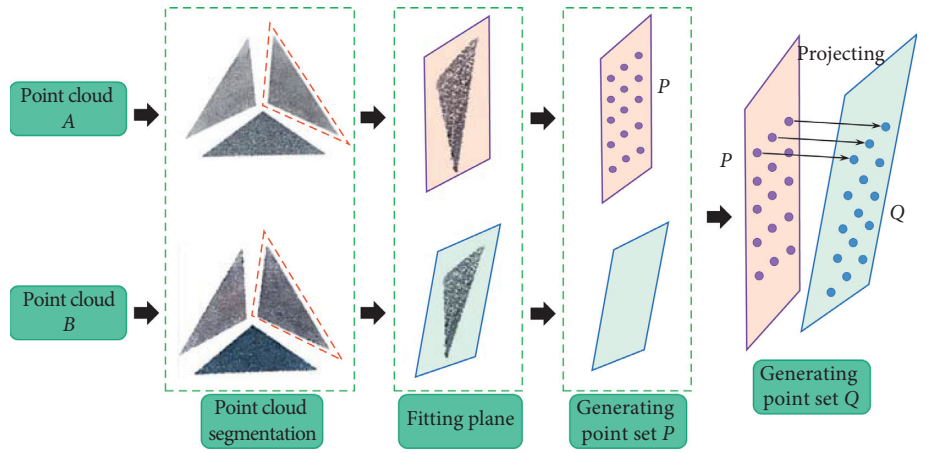

Figure 3: Precise registration process of a triangular pyramid marker.

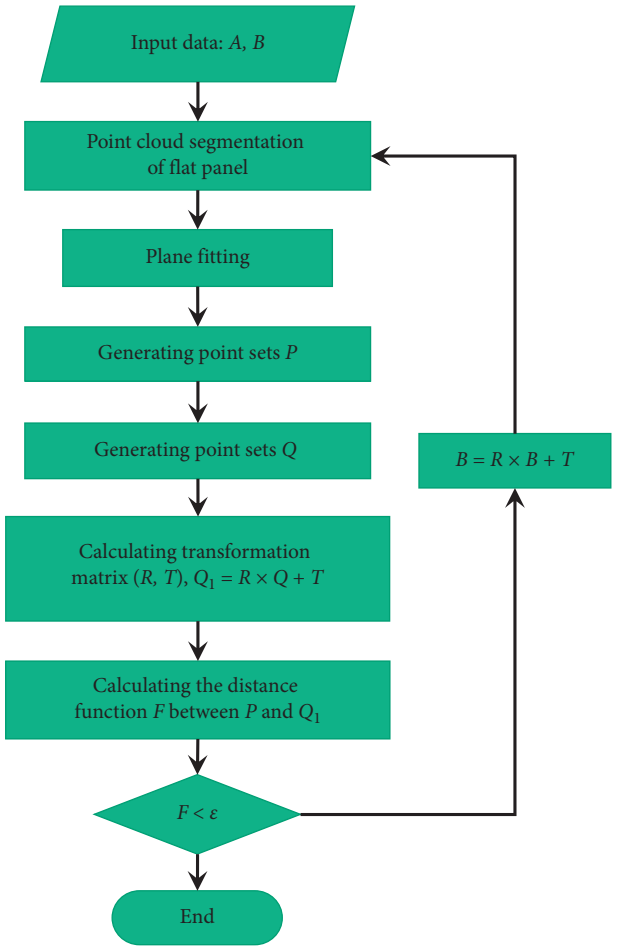

Figure 4: Iterative process of the transformation parameters.

$$C_p = \frac{1}{n}\sum_{i=1}^{n} p_i,$$
$$C_q = \frac{1}{n}\sum_{i=1}^{n} q_i, \tag{3}$$

where n is the number of point sets. Then, the covariance between point sets P and Q is calculated.

$$E = \frac{1}{n}\sum_{i=1}^{n}\left[\left(p_i - C_p\right)\left(q_i - C_q\right)^T\right]. \tag{4}$$

The symbol E is decomposed as follows: $E = UV^T$. Then, the rotation and translation matrices can be calculated using formula

$$R = UV^T,$$
$$T = C_p - RC_q. \tag{5}$$

The distance function F can be described by the sum of the square of the point distance, the average point distance, and the maximum point distance. Point sets P and Q are generated on the fitting plane; thus, determining the final registration accuracy by using the maximum point spacing is more intuitive and accurate than using the iterative convergence standard ε.

3.3. Accuracy Verification Experiment. An experiment is designed to verify accuracy by using the proposed method. In the experiment, a triangular pyramid marker, a spherical marker, and ICP are used. Figure 5(a) shows the experimental objects, which are three typical geometries (cylinder, sphere, and cube). The triangular pyramid and spherical markers are placed in approximately the same position, as shown in Figure 5(b). Three groups of registration markers are placed around the experimental objects. One scan is performed on each side of the experimental objects, as shown in Figures 6(a) and 6(b). The point clouds of the three groups of markers are completely collected in both scans. The registered point cloud is depicted in Figure 6(c).

In general, resolution is defined as the distance between points on a spherical surface 10 m away from the scanner. In this experiment, three types of contrast scanning with different resolutions (1.6, 3.1, and 6.3 mm) are performed. The actual dimensions of the experimental objects are accurately measured using a vernier caliper. The measured radius of the cylinder is 37.14 mm, the radius of the sphere is 83.16 mm,

(a) (b)

Figure 5: Verification experiment on registration accuracy: (a) three typical geometries used to verify registration accuracy and (b) triangular pyramid and spherical markers.

and the side length of the cube is 149.94 mm. The experimental objects are separated from the point cloud after using three different methods to register the point cloud. Cylinder, sphere, and plane fitting algorithms are used to calculate the geometric dimensions of the experimental objects. The geometric deviations of the three registration methods are determined at different resolutions by comparing the geometric dimensions obtained via point cloud calculation with the measured dimensions, as shown in Figure 7. The inaccurate registration of the point cloud will change the geometric shape of the experimental objects, resulting in errors in the calculation of geometric dimensions. Therefore, geometric errors can reflect the registration accuracy of the point cloud. As shown in Figure 7, achieving submillimeter registration accuracy is difficult for the ICP algorithm. In addition, when the original point cloud is used directly for registration, ICP always fails due to insufficient overlap. In this experiment, a large number of nonoverlapping parts of the point cloud are artificially deleted, and thus, ICP can converge to the correct result. Therefore, the ICP algorithm is not applicable to VTA. Compared with ICP, the registration accuracy of the spherical marker is significantly improved. However, the geometric errors of all three experimental objects exceed 1 mm when the resolution is 6.3 mm. Compared with those of existing registration methods, the registration accuracy of the proposed registration method is significantly improved. Under the three resolution conditions, the geometric deviation of all the experimental objects is less than 1 mm. Overall, the proposed registration algorithm and triangular pyramid markers can make the prediction result of VTA more accurate and reliable.

4. Accurate Simulation of Mechanical State in VTA

4.1. Case Introduction. For some large-scale structures with complex loads, such as arch bridges, the shape and stress of the structure must be strictly controlled after assembly. The initial stress deviation directly causes structural safety to decrease. Therefore, a complete VTA should have the capability to predict the initial stress and shape deviation of the assembled structure. A reduced-scale steel tube arch bridge is designed to simulate the actual bridge assembly process. The detailed dimensions are presented in Figure 8. The arch bridge is composed of five identical prefabricated segments connected by bolts. Each connection end has four bolts. Similar to the actual structure, geometric deviations may occur in each prefabricated segment due to the welding process. The proposed VTA procedure has three important contents: (1) the acquisition of high-precision point clouds of prefabricated segments, (2) the precise construction or modification of the BIM of a prefabricated segment on the basis of the scanned point cloud, and (3) the use of Abaqus to simulate the actual assembly process accurately on the basis of the accurate BIM. A Leica P50 scanner is used to obtain the point cloud of a prefabricated segment of the experimental arch bridge. The prefabricated segments are placed as shown in Figure 9(a). Four scans with a scan resolution of 3.1 mm are performed around the prefabricated segments. The scan scene is shown in Figure 9(b). Three triangular pyramid markers are placed in the scanning field of view. The complete point cloud obtained using the proposed point cloud registration method is shown in Figure 9(c). Meanwhile, Figure 9(d) presents a prefabricated segment point cloud segmented from the overall point cloud.

4.2. Creating BIM Based on Point Clouds. A BIM of the prefabricated components is necessary in VTA. Although BIMs have been adopted in many projects, they are ideal unbiased models. Updating or reconstructing BIM on the basis of point clouds is essential. When the existing BIM cannot be driven by parameters, the BIM for VTA should be completely derived from point clouds through reverse engineering. During the assembly process, the geometric parameters (e.g., shape and attitude) of PCs will change. Therefore, the use of a parametric modeling method is suggested in reverse engineering. For common slender components in steel structures, the design centerline is typically a specific function curve, such as a straight line, a catenary, and a circular arc. The centerline deviation caused by welding deformation and nonlinear effect during physical assembly is irregular. However, the parametric form used to describe the idealized design intent in conventional BIM software (e.g., Autodesk Revit, SolidWorks, Rhino3D, and ArchiCAD) is not conducive to the irregular shape of the centerline.

Therefore, a parameter-driven modeling method that can approximate any curve should be developed when establishing the BIM of curved components. The suggested method is using a multipoint spline curve. Figure 10 illustrates the modeling steps of the experimental arch bridge. The detailed algorithm steps are as follows:

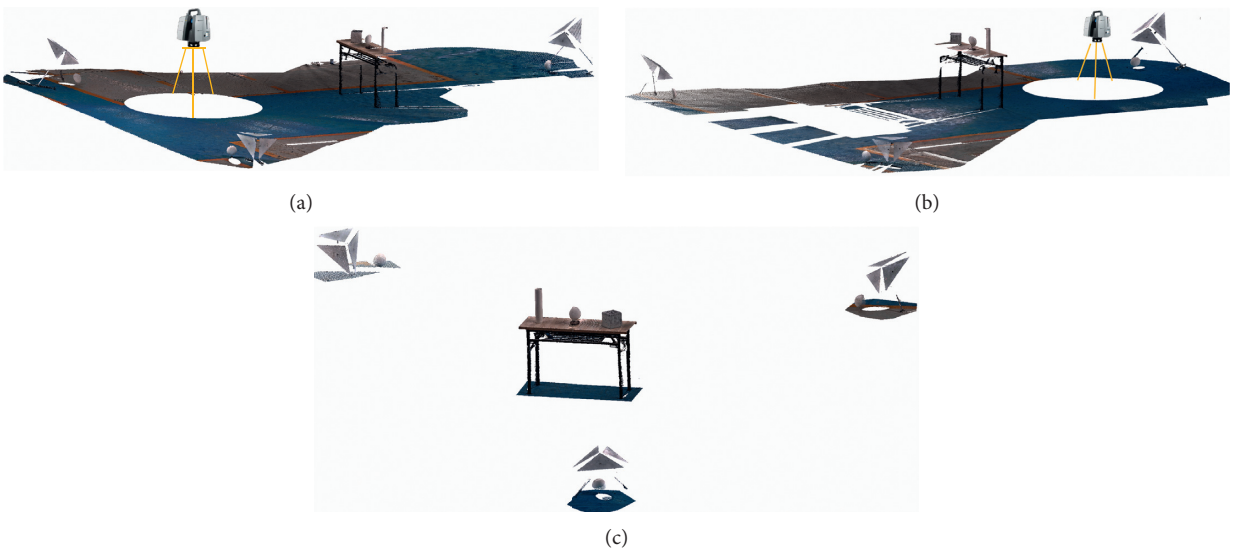

(a) (b) (c)

Figure 6: Scanning point cloud of verification experiment: (a) scanning point cloud 1, (b) scanning point cloud 2, and (c) point cloud after accurate registration.

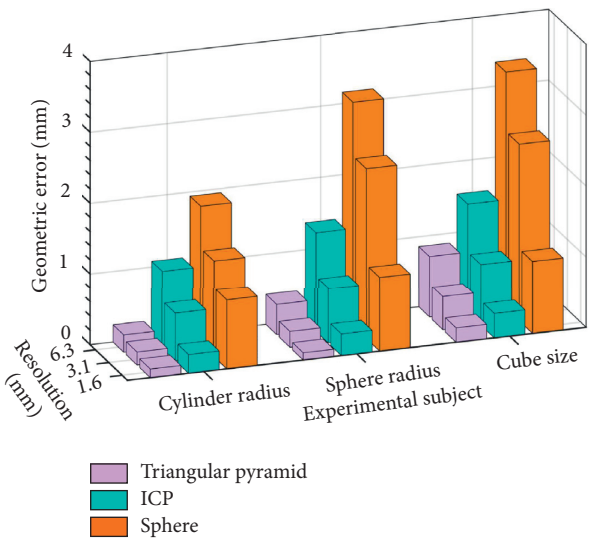

Figure 7: Geometric deviation of the experimental objects.

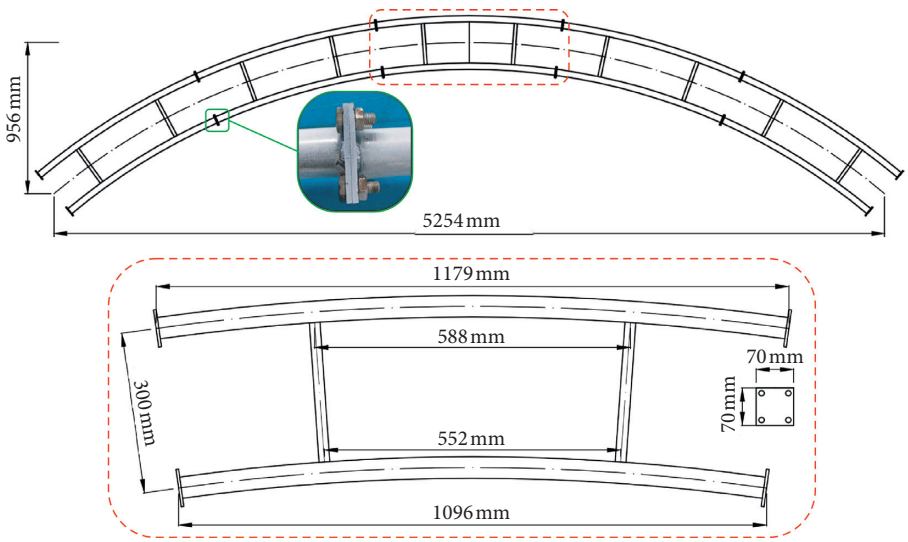

Figure 8: Design drawing of the scaled arch bridge.

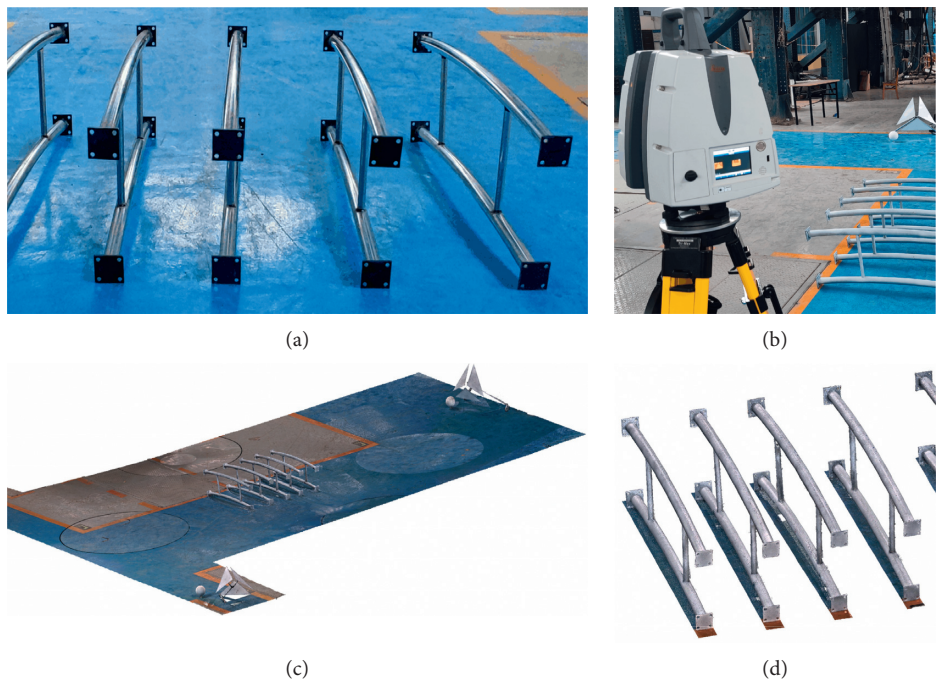

FIGURE 9: Scanning of the scaled arch bridge: (a) prefabricated segment, (b) on-site scanning, (c) registered point cloud, and (d) prefabricated segment point cloud segmentation.

Step 1: The point cloud of the curve component is segmented from the overall point cloud.

Step 2: A high-order polynomial is used to preliminarily fit the curve shape of the point cloud of a curve component.

Step 3: The tangential vector of any point (x_i, y_i, and z_i) can be obtained on the fitting polynomial curve. At (x_i, y_i, and z_i), a point cloud is cut along the tangential vector.

Step 4: The local coordinate system is established by the normal plane of the tangential direction and the tangential vector.

Step 5: The point cloud is projected onto the normal plane in the local coordinate system. Then, the point cloud is fitted with a plane circle to obtain the coordinate parameters of the center point i and the radius parameters R of the circle.

Step 6: In the BIM software, the BIM of the curve component is constructed using spline curves based on point i and radius R.

In a steel structure connected by bolts, the assembly method of PCs is typically face to face with multiple bolts. The alignment of the center of all the bolt holes and the surface-to-surface fit constitute the mandatory geometric constraints of the connection joints. Therefore, the BIM of the connection joints of a PC should be accurately constructed before virtual assembly. In general, the number of bolts that connect joints is large; thus, an automated program is required to calculate the center coordinates of the bolt holes from the point cloud. Li et al. proposed a method for segmenting circular holes in laser point cloud data for precast concrete stair components [36]. Their method determines the boundary points of the bolt holes by traversing and calculating the geometric relationship between each point and the points in its adjacent area. Although the method of Li et al. is simple and effective, traversing all points consumes considerable computing resources. The current study proposes a more efficient algorithm, and its key steps are presented in Figure 11. First, grid points are generated in the point cloud. The spacing of the grid points is **d**, as shown in Figure 11(a). The best value of **d** is the diameter of the bolt hole to ensure that each possible bolt hole area has a grid point. Then, the nearest points **A**, **B**, **C**, and **D** of each grid point M_i are calculated in the X-direction and the Y-direction to obtain the two chords **AB** and **CD** of the bolt hole. When M_i is located in the bolt hole area, at least one of the lengths of **AB** and **CD** is greater than $\sqrt{2}/2\mathbf{d}$, and neither is greater than **d**. The bolt area can be searched quickly on the basis of these geometric characteristics. In accordance with the geometric characteristics of a circle, the intersection $\mathbf{O_0}$ of the vertical lines **EF** and **GH** of **AB** and **CD** is the center of the bolt hole, as shown in Figure 11(b). However, $\mathbf{O_0}$ is only calculated on the basis of four random points **A**, **B**, **C**, and **D**, and it may have excessive random errors. Furthermore, the point cloud is converted into a polar coordinate system with $\mathbf{O_0}$ as the origin. The coordinates of each point in the point cloud are transformed into ($\boldsymbol{\theta}$, $\mathbf{r}$). In the interval of $\boldsymbol{\theta} + \Delta\boldsymbol{\theta}$, the point with the smallest r is the boundary point of the circular hole. Finally, circle fitting is performed on the boundary points to obtain the

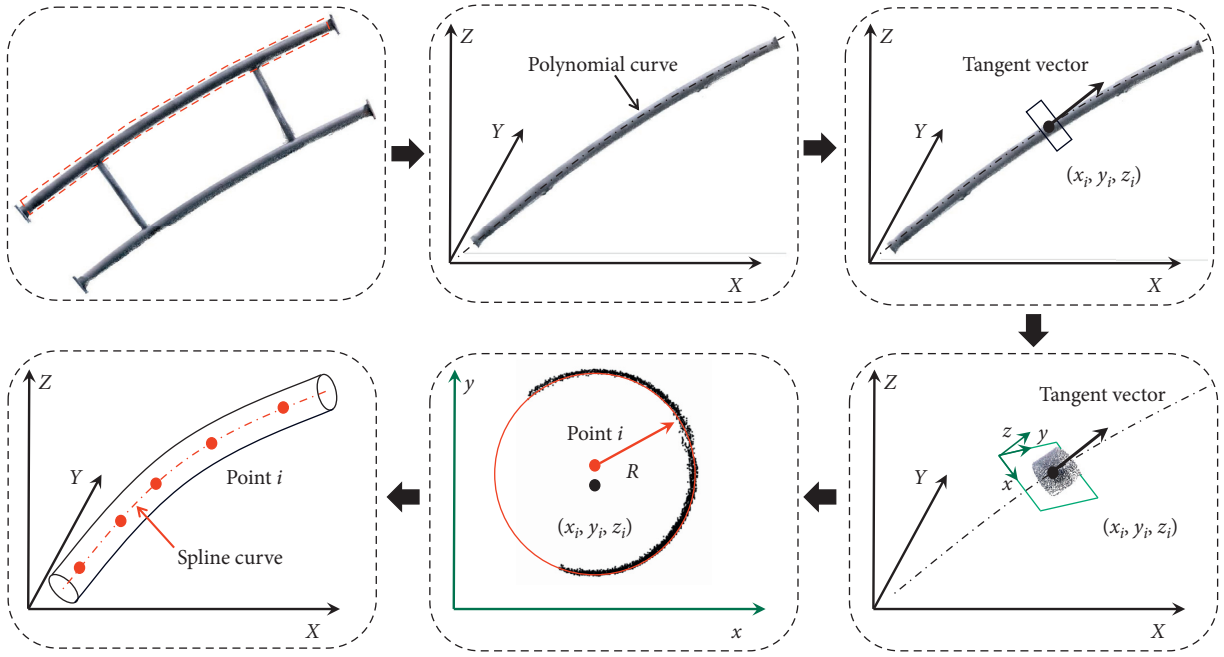

Figure 10: Reverse construction of the building information modeling steps of curved components.

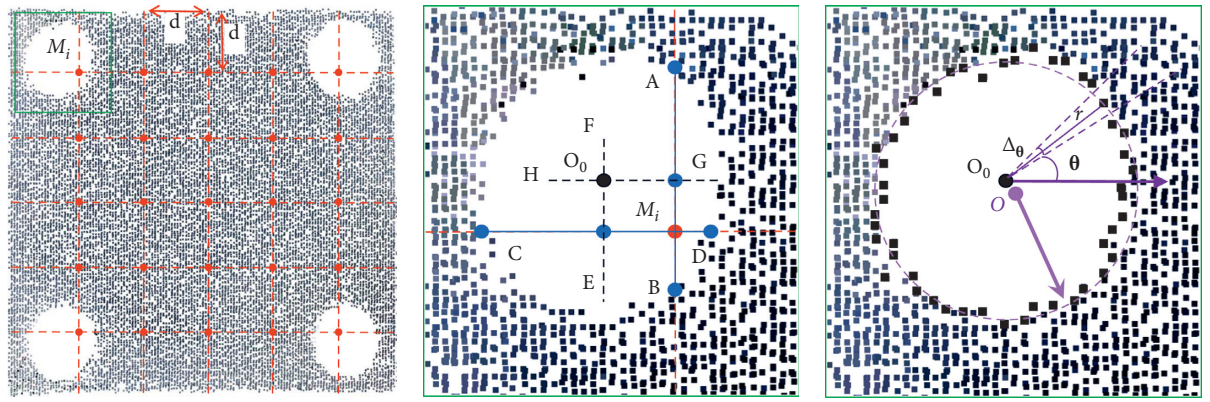

(a) (b) (c)

Figure 11: Example of the calculation process of the bolt hole center: (a) generate grid points, (b) calculate the circle center $\mathbf{O_0}$, and (c) calculate the circle center (O).

calculation center **O** of the bolt hole, as shown in Figure 11(c). The advantage of the proposed method is that the bolt hole area can be searched quickly, and the boundary point is searched only in the area near the bolt hole. The algorithm considerably improves computational efficiency while ensuring accuracy.

When the BIM of connecting joints is constructed reversely, the central coordinates of bolt holes should be parameterized. The models of bolt holes are updated automatically when the central coordinates of bolt holes are updated. For the flange plate wherein the bolt hole is located, determining the position and spatial inclination of the plane through the point cloud fitting plane is necessary.

4.3. Forced Assembly Simulation Method. If the connection joints of PCs have machining errors, then the structure inevitably deforms during the process of installing bolts. Figure 11 shows a schematic of the bolt assembly process. When no geometric deviation of a PC occurs, the adjacent flange plate will fit naturally and tightening the bolts will exert no effect on the shape of the assembly, as shown in Figure 12(a). When geometric deviations occur in the connection joints of the PC, as shown in Figure 12(b), the process of tightening the bolts will cause the gaps $\mathbf{e_1}$, $\mathbf{e_2}$, $\mathbf{e_3}$, and $\mathbf{e_4}$ between the joints to disappear gradually. Finally, the flange plate is fitted fully and causes additional deformation, as shown in Figure 12(c). When only the BIM is used, gaps $\mathbf{e_1}$, $\mathbf{e_2}$, $\mathbf{e_3}$, and $\mathbf{e_4}$ cannot become zero

simultaneously during rigid transfer even if the BIM is accurately constructed. Therefore, an accurate simulation of elastic deformation is essential. Before the simulation of elastic deformation, a rigid transformation is implemented in the BIM system to achieve preliminary joint alignment. The process of aligning a large number of bolt holes is similar to the point cloud registration process. The use of formulas (3)–(5) can accelerate the initial assembly process.

As early as 1996, Choi et al. developed a simple and effective contact algorithm for simulating the interaction between flanges. At present, contact boundary has been widely integrated into mainstream finite element analysis systems (e.g., Ansys and Abaqus FEA). The existing common method for simulating bolt tightening is to apply a pretightening force to the bolt and use the surface-to-surface contact of the flange plate as the boundary condition. Although this method reduces the difficulty in preprocessing the finite element model, the time of the finite element solution increases considerably, and the iterative solution is difficult to converge. In particular, when virtual assembly of multiple PCs is performed simultaneously, contact analysis requires considerable computing resources and may enter the wrong state of convergence. The suggested method is to simulate the assembly gap with the connection displacement. The geometric parameter transfer and transformation are clear during the entire process because the coordinates of the bolt holes on the flange plate are accurately obtained using the point cloud and the initial assembly is completed in the BIM system. That is, the gap between the bolt pairs at any connecting joint is known. Simultaneously, the geometric model used in Abaqus is a BIM after preliminary assembly. Therefore, only setting the displacement of the connecting element to the negative of the gap is necessary. Using Figure 12(b) as an example, a connecting element is established in Abaqus between each pair of bolt holes; the displacement values of the connecting element are $-\mathbf{e_1}$, $-\mathbf{e_2}$, $-\mathbf{e_3}$, and $-\mathbf{e_4}$. The actual gap in the model will be zero when the solution is completed. This state is essentially the same as the surface-to-surface contact of the flange plate. Figure 13 shows the finite element model of the experimental arch bridge. The bolts of each connection joint are simulated via connection displacement. Given that the BIM is an accurate solid model, solid elements are used directly to divide the mesh.

A verification experiment is designed to prove the accuracy of the proposed gap simulation method. First, all the segments of the experimental arch bridge are assembled into a whole and the bolts are tightened completely. The initial shape of the experimental arch bridge is obtained via 3D scanning, as shown in Figure 14(a). Then, metal gaskets are added between the connection joints of the lower chord between the second and third segments. The total thickness of the gaskets is $\boldsymbol{\delta}$, as shown in Figure 14(b). The bolts are tightened again after adding the gasket. The experimental arch bridge is rescanned to obtain the new shape of the arch bridge. The measured change in arch rib shape is caused by the forced displacement of δ between the bolt pairs. Simultaneously, the corresponding connection displacement in the finite element is set to $\boldsymbol{\delta}$ to obtain the predicted shape change, as shown in Figures 14(c) and 14(d). A unified reference point is required to compare the measured shape change with the predicted shape change. In the finite element model, the upper arch foot on the left is set as a fixed constraint. For the actual arch, the upper arch foot on the left is also set as the zero points of translational deformation and corner deformation.

Figure 15 shows the deformation caused by different degrees of artificial forced displacement. When the forced displacement is $\delta = 2$ mm, the deformation predicted by the finite element and the deformation measured via scanning are shown in Figure 15(a). The deformation result of $\delta = 4$ mm is presented in Figure 15(b). As shown in the figure, the deformation predicted via FEM exhibits good agreement with the actual deformation of the structure. Within the range of 0–3 m in the horizontal direction, the predicted and measured deformation curves nearly overlap completely. The largest deformation deviation occurs in the right arch. When $\delta = 2$ mm, the maximum displacement deviation is 1.9 mm, accounting for 7.6% of the total displacement. When $\delta = 4$ mm, the maximum displacement deviation is 3.2 mm, accounting for 6.4% of the total displacement. In addition, the measured deformations are all smaller than the predicted values. Overall stiffness is stronger than that of the finite element model because the thickness or elastic modulus of the actual structure may be larger than the designed value. In general, the proposed forced assembly simulation method is proven to be reliable.

5. VTA Framework and Experimental Validation

In accordance with the research conclusions presented in this work, a general methodology framework of VTA is proposed for steel structures with bolt forced assembly, as shown in Figure 16.

Considering the manufacturing errors of the prefabricated segments of the experimental arch bridge, virtual assembly is performed in accordance with the proposed process to verify the accuracy and reliability of the proposed method. In particular, accuracy is verified by comparing the VTA-predicted geometry with that of the actual assembly. Figure 17(a) shows the geometry of the five prefabricated segments of the experimental bridge after VTA and after actual assembly. Figure 17(b) presents the shape deviation after VTA and the actual assembly. The results indicate that the prediction error of the proposed VTA method is within 0.003 m. The maximum prediction deviation value is only 1/1800 of the bridge span. The primary causes of these prediction deviations may be (1) the calculation errors of flange plate inclination and bolt hole center coordinates and (2) discrepancies in stiffness between the actual structure and the finite element model. As shown in Figure 17(b), the local peak noise is generated when calculating the centerline of the arch rib based on the point cloud. It is mostly present in the connections between the flange plate and the connecting rod. However, these noises do not affect overall geometry.

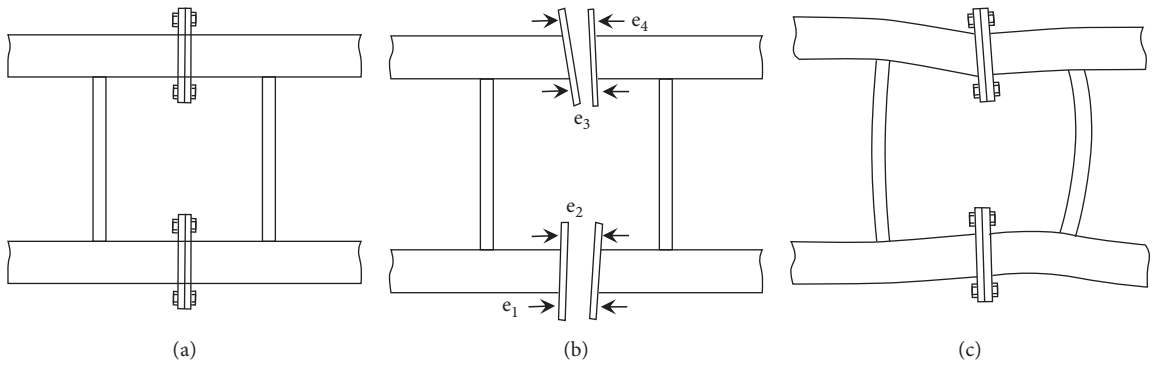

Figure 12: Bolt assembly process: (a) theoretical assembly, (b) assembly clearance, and (c) forced assembly.

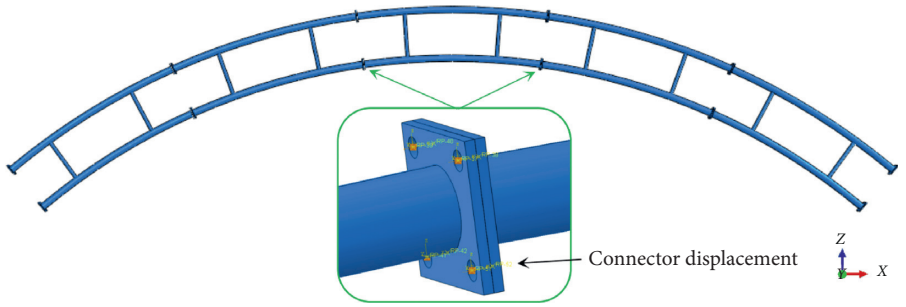

Figure 13: Finite element model of the experimental arch bridge.

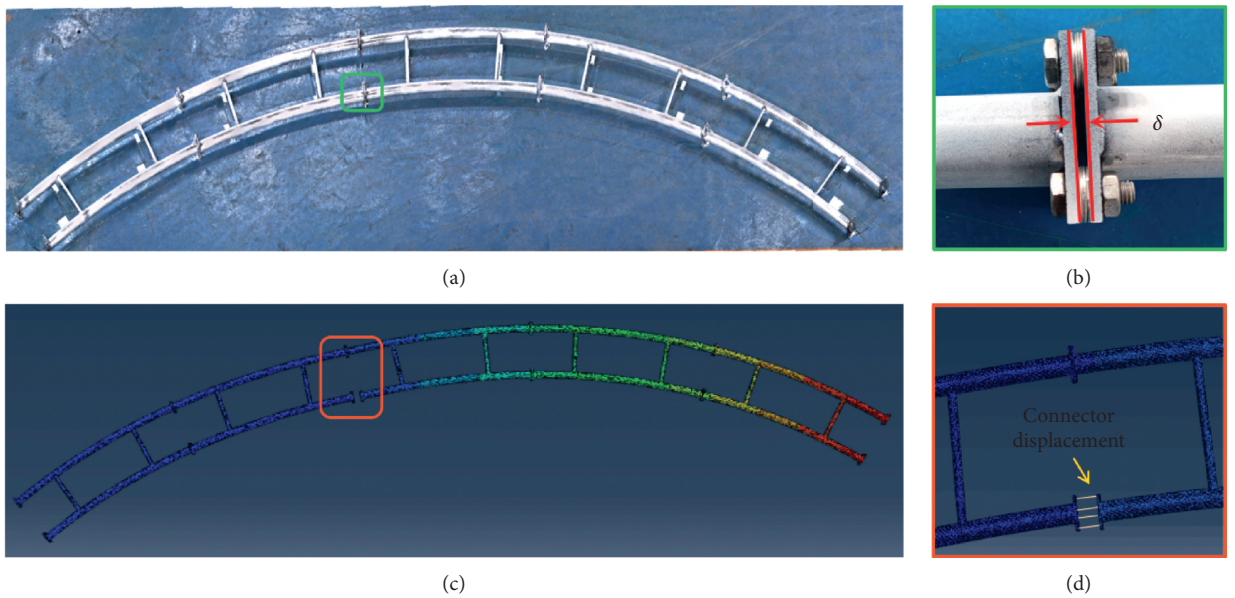

Figure 14: Gap simulation verification experiment: (a) overall scanning point cloud of the arch bridge, (b) gap σ, (c) shape predicted via FEM, and (d) connection displacement.

Minimal initial stress is generated in the structure after complete assembly given that the manufacturing errors in the prefabricated segments of the experimental bridge are insignificant. To demonstrate that the proposed VTA method can accurately predict initial stresses induced during forced assembly, metal gaskets with a thickness (δ) of 6 mm are artificially added by installing them in the same position and manner shown in Figure 14. Stress

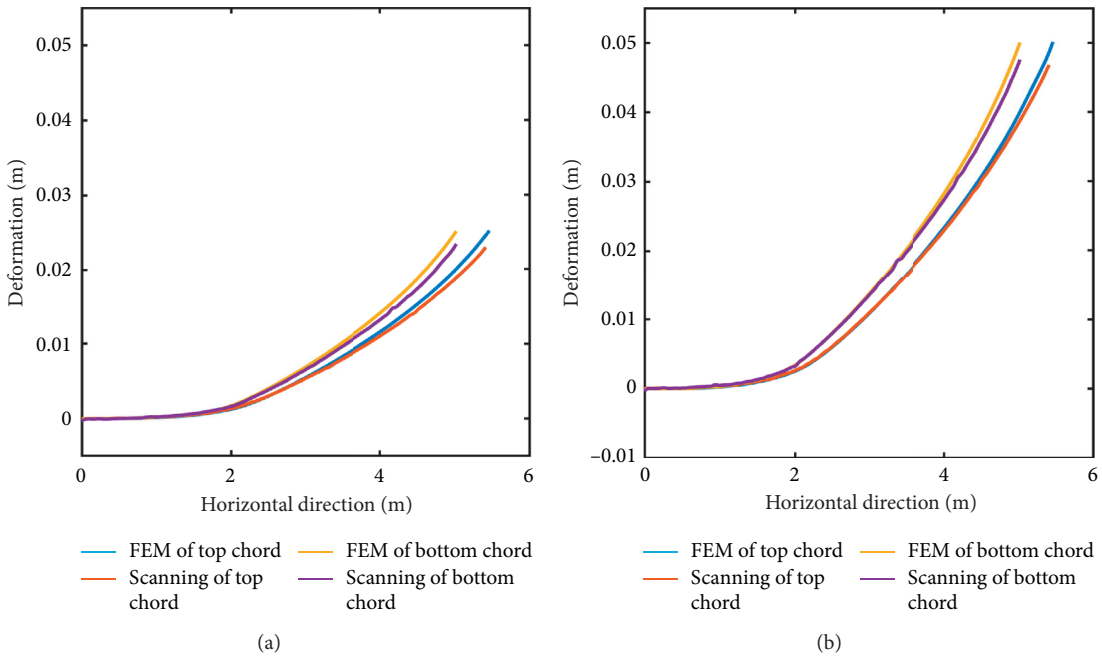

Figure 15: Deformation caused by forced displacement: (a) $\delta = 2$ mm and (b) $\delta = 4$ mm.

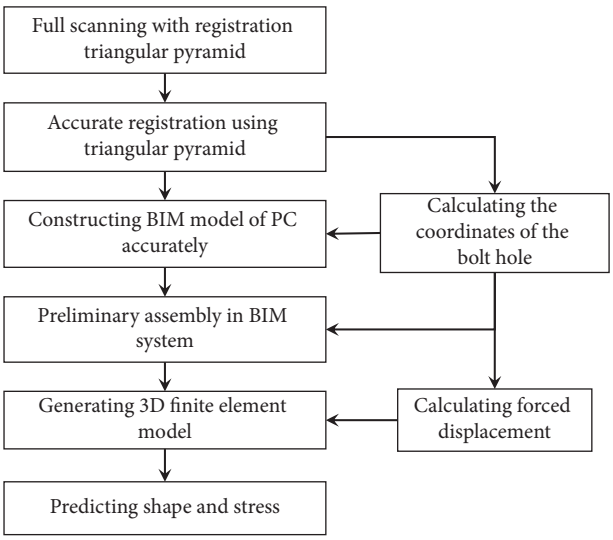

Figure 16: Proposed VTA process.

sensors are arranged in the position shown in Figure 18(a) to measure the initial stresses in the structure after assembly. Meanwhile, Figure 18(b) presents the forecast geometric error of VTA. For the experimental bridge, significant elastic deformation is induced when δ reaches 6 mm. Compared with that in Figure 17(b), no significant increase in error occurs in VTA. Figure 18(c) depicts the initial stress predicted via VTA and the measured value, with a mean of 85.05 MPa and 94.07 MPa, respectively. The deviation of predicted stress may be accounted for by the greater stiffness of the actual structure, which typically causes less deformation under higher stress level. By contrast, forced displacements are equal in VTA and in practice, and thus, stress levels are higher in more rigid structures. Overall, the mean value of stress predicted via VTA reached 90% of the mean value of the measured stress, indicating the high accuracy of stress prediction using VTA.

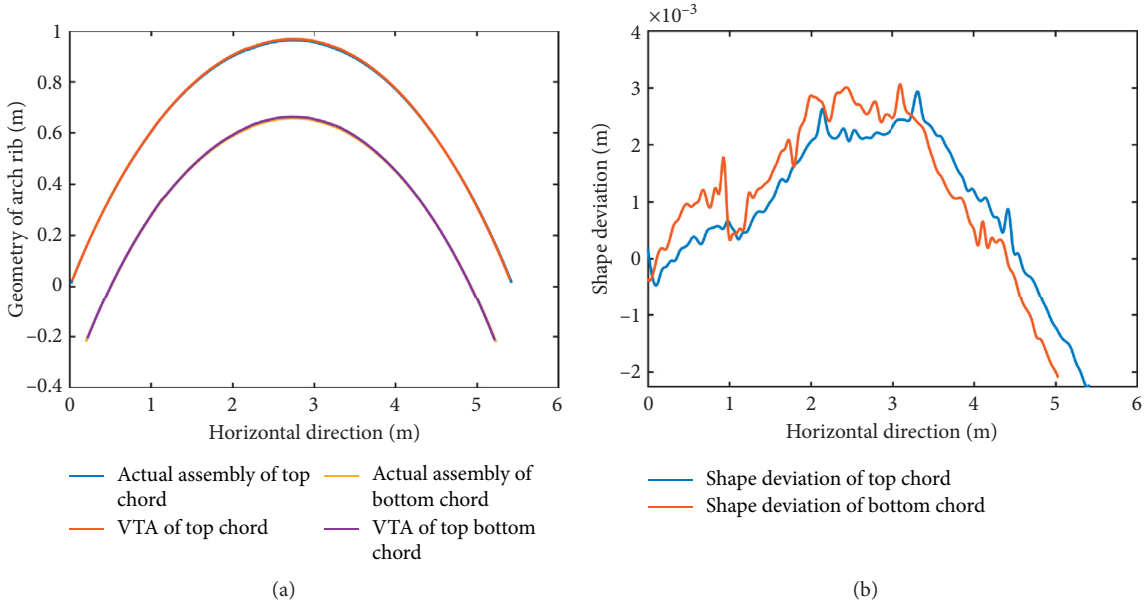

Figure 17: Results of the VTA for the experimental arch bridge: (a) geometry of the arch ribs and (b) geometric deviation.

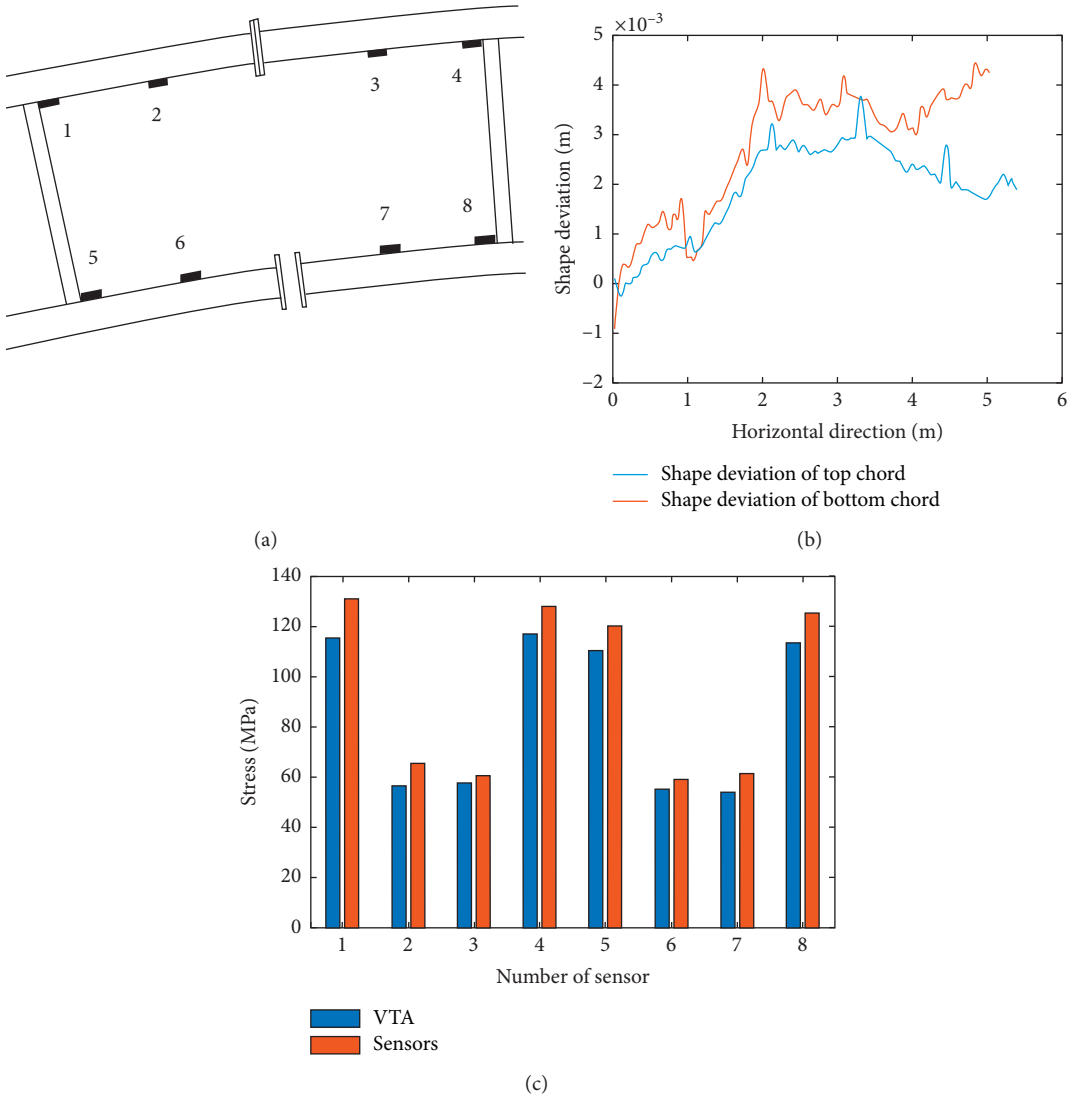

Figure 18: VTA experimental results ($\delta = 6$ mm): (a) stress sensor arrangement, (b) geometric deviation, and (c) stress results.

6. Conclusion

In industrial construction, the implementation of VTA can effectively reduce the cost and time limit of PC buildings and predict the risks involved in the assembly process. The major contributions of this research include the following: (1) a general methodology framework for the VTA of forced assembly steel structures with bolted connections is introduced, (2) an accurate point cloud registration method based on a triangular pyramid that can achieve submillimeter registration accuracy is developed, and (3) a simulation method that considers the mechanical state for tightening bolts and that can accurately predict the deformation and stresses caused by forced assembly is proposed. The principal findings of this study are as follows:

(1) The registration method of the point cloud exerts a significant effect on registration accuracy. The experimental results indicate that the accuracy of the proposed registration method is better than that of the registration sphere and ICP algorithms.

(2) A detailed 3D finite element analysis is necessary for structures with forced assembly. Accurately building and correcting BIMs on the basis of point cloud inversion are crucial. This study develops efficient parameter extraction algorithms for curved members and bolted connection joints that help reduce manual work in VTA.

(3) The use of connection displacements instead of face contact boundaries to simulate flange plate closure in finite elements can considerably reduce time and computational resources required for model analysis. This simulation method is not limited to the use of connection displacements in Abaqus. The same effect can be achieved by varying the lengths of an element by using temperature loads.

For the case in which multiple components are assembled end to end, such as the arch bridge in this paper, a small systematic error in a point cloud exerts a considerable effect on the prediction results of VTA. This study uses Leica P50 (a high-precision and heavy-duty TLS) and a new point cloud registration method to reduce the systematic error of point clouds. Therefore, mobile scanners and light-duty TLS are not recommended for accurate VTA due to the large systematic error of the instrument itself. The proposed method is not limited to bridge structures, but it is also applicable to steel structures in buildings. However, the feasibility of VTA still requires further study for prefabricated concrete components because of different assembly rules. In addition, the individual programs of VTA still run independently. In future applications, the development of systems that integrate point cloud registration, model construction, and virtual assembly will help improve the automation of industrial construction.

Data Availability

The data used to support the findings of this study are included within the article.

Conflicts of Interest

The authors declare that there are no conflicts of interest regarding the publication of this paper.

Acknowledgments

This research was funded by the Chongqing Smart City and Sustainable Development Academy.

References

[1] H. Bachmann, A. Steinle, and P. Thrift, *Prefabricated Concrete Structures*, Ernst & Sohn, Berlin, Germany, 2019.

[2] A. A. Yee, "Social and environmental benefits of precast concrete technology," *PCI Journal*, vol. 46, no. 3, pp. 14–19, 2001.

[3] F. Case, A. Beinat, F. Crosilla, and I. M. Alba, "Virtual trial assembly of a complex steel structure by generalized Procrustes analysis techniques," *Automation in Construction*, vol. 37, pp. 155–165, 2014.

[4] P. Delmas and T. Gee, "Stereo camera visual odometry for moving urban environments," *Integrated Computer-Aided Engineering*, vol. 26, no. 3, pp. 243–256, 2019.

[5] T. C. Lukins and E. Trucco, "Towards automated visual assessment of progress in construction projects," in *Proceedings of the British Machine Vision Conference (BMVC)*, pp. 142–151, University of Warwick, Coventry, UK, September 2007.

[6] L. Song, "Project progress measurement using CAD-based vision system," in *Proceedings of the ASCE Construction Research Congress A Global Community*, ASCE, Grand Bahama Island, The Bahamas, May 2007.

[7] F. Bosché, M. Ahmed, Y. Turkan, C. T. Haas, and R. Haas, "The value of integrating scan-to-BIM and scan-vs-BIM techniques for construction monitoring using laser scanning and BIM: the case of cylindrical MEP components," *Automation in Construction*, vol. 49, pp. 201–213, 2015.

[8] H. S. Park, H. M. Lee, H. Adeli, and I. Lee, "A new approach for health monitoring of structures: terrestrial laser scanning," *Computer-Aided Civil and Infrastructure Engineering*, vol. 22, no. 1, pp. 19–30, 2007.

[9] Z. Ma and S. Liu, "A review of 3D reconstruction techniques in civil engineering and their applications," *Advanced Engineering Informatics*, vol. 37, pp. 163–174, 2018.

[10] C. Rausch, M. Nahangi, and M. Perreault, "Optimum assembly planning for modular construction components," *Journal of Computing in Civil Engineering*, vol. 31, no. 1, Article ID 04016039, 2016.

[11] M. K. Kim, Q. Wang, J. W. Park, J. C. Cheng, H. Sohn, and C. C. Chang, "Automated dimensional quality assurance of full-scale precast concrete elements using laser scanning and BIM," *Automation in Construction*, vol. 72, pp. 102–114, 2016.

[12] C. Rausch, R. Lu, S. Talebi, and C. Haas, "Deploying 3D scanning based geometric digital twins during fabrication and assembly in offsite manufacturing," *International Journal of Construction Management*, vol. 6, pp. 1–14, 2021.

[13] W. Wang, J. Wang, and G. Sun, "Noise reduction and modeling methods of TLS point cloud based on R-tree," in

Proceedings of the IEEE 2009 Joint Urban Remote Sensing Event, Shanghai, China, May 2009.

[14] D. Bolkas and A. Martinez, "Effect of target color and scanning geometry on terrestrial LiDAR point-cloud noise and plane fitting," *Journal of Applied Geodesy*, vol. 12, no. 1, pp. 109–127, 2017.

[15] W. Huang and Z. Kong, "Simulation and integration of geometric and rigid body kinematics errors for assembly variation analysis," *Journal of Manufacturing Systems*, vol. 27, no. 1, pp. 36–44, 2008.

[16] A. Diosi and L. Kleeman, "Laser scan matching in polar coordinates with application to SLAM," in *Proceedings of the IEEE/RSJ International Conference on Intelligent Robots and Systems*, pp. 3317–3322, Shaw Convention Center-Edmonton, Edmonton, Canada, August 2005.

[17] D. Holz and S. Behnke, "Sancta simplicitas—on the efficiency and achievable results of SLAM using ICP-based incremental registration," in *Proceedings of the IEEE International Conference on Robotics and Automation*, pp. 1380–1387, Anchorage, AK, USA, May 2010.

[18] J. Rowekamper, C. Sprunk, and C. Stachniss, "On the position accuracy of mobile robot localization based on particle filters combined with scan matching," in *Proceedings of the IEEE/RSJ International Conference on Intelligent Robots and Systems*, pp. 3158–3164, Algarve, Portugal, October 2012.

[19] Z. Kang, L. Tuo, and S. Zlatanova, "Continuously deformation monitoring of subway tunnel based on terrestrial point clouds," in *Proceedings of the XXII Congress of the International Society for Photogrammetry and Remote Sensing (ISPRS), IAPRS XXXIX-B5*, Melbourne, Australia, September 2012.

[20] J.-Y. Han, J. Guo, and Y.-S. Jiang, "Monitoring tunnel deformations by means of multi-epoch dispersed 3D LiDAR point clouds: an improved approach," *Tunnelling and Underground Space Technology*, vol. 38, pp. 385–389, 2013.

[21] Y. Chen and G. Medioni, "Object modeling by registration of multiple range images," in *Proceedings of the IEEE International Conference on Robotics and Automation*, vol. 3, pp. 2724–2729, Sacramento, CA, USA, April 1991.

[22] P. J. Besl and N. D. McKay, "A method for registration of 3-D shapes," *IEEE Transactions on Pattern Analysis and Machine Intelligence*, vol. 14, no. 2, pp. 239–256, 1992.

[23] W. Xin and J. Pu, "An improved ICP algorithm for point cloud registration," in *Proceedings of the International Conference on Computational and Information Sciences*, pp. 565–68, Chengdu, China, December 2010.

[24] K. Low, "Linear least-squares optimization for point-to-plane ICP surface registration," Technical Report TR04–004, Department of Computer Science, University of North Carolina, Chapel Hill, NC, USA, 2004.

[25] S. Azhar, A. Nadeem, J. Y. N. Mok, and B. H. Y. Leung, "Building information modeling (BIM): a new paradigm for visual interactive modeling and simulation for construction projects," in *Proceedings of the First International Conference on Construction in Developing Countries (ICCIDCI)*, Karachi, Pakistan, August 2008.

[26] S. Azhar, M. Hein, and B. Sketo, "Building information modeling (BIM): benefits, risks and challenges," in *Proceedings of the International 44th Annual Conference of the Associated Schools of Construction*, pp. 1–11, Auburn University, Auburn, AL, USA, April 2008.

[27] N. Lu and T. Korman, "Implementation of building information modeling (BIM) in modular construction: benefits and challenges," in *Proceedings of the Construction Research Congress*, pp. 1136–1145, Banff, Canada, May 2010.

[28] L. Joosung and K. Jaejun, "BIM-based 4D simulation to improve module manufacturing productivity for sustainable building projects," *Sustainability*, vol. 9, no. 3, p. 426, 2017.

[29] X. Gao, D. Zhou, and W. Cui, "Application of 3D laser scanning combined with BIM technology in 3D modeling of ancient buildings," *Surveying and Mapping Bulletin*, vol. 5, pp. 158–162, 2019.

[30] M. Pepe, D. Costantino, and A. R. Garofalo, "An efficient pipeline to obtain 3D model for HBIM and structural analysis purposes from 3D point clouds," *Applied Sciences*, vol. 10, no. 4, pp. 12–35, 2020.

[31] B. Deng, Z. Wang, and Y. Jin, "Feature extraction method of laser scanning point cloud based on morphological gradient," *Laser and Optoelectronics Progress*, vol. 55, no. 5, pp. 239–245, 2018.

[32] V. Verma, R. Kumar, and S. Hsu, "3D building detection and modeling from aerial LIDAR data," in *Proceedings of the IEEE Computer Society Conference on Computer Vision and Pattern Recognition*, vol. 2, pp. 2213–2220, New York, NY, USA, June 2006.

[33] D. Jiang, G. Na, and K. Ji, "Research on assembly model based on assembly constraints transformation," *Procedia Engineering*, vol. 29, pp. 770–774, 2012.

[34] Y. Zhou, W. Wang, H. Luo, and Y. Zhang, "Virtual pre-assembly for large steel structures based on BIM, PLP algorithm, and 3D measurement," *Frontiers of Engineering Management*, vol. 6, no. 2, pp. 207–220, 2019.

[35] C. Ying, Y. Zhou, D. Han, G. Qin, K. Hu, and T. Guo, "Applying BIM and 3D laser scanning technology on virtual pre-assembly for complex steel structure in construction," in *Proceedings of the CCESEM2019*, IOP Publishing Ltd., Beijing, China, Article ID 022036, p. 8, September 2019.

[36] D. Li and J. Liu, "Automatic modeling of prefabricated components with laser-scanned data for virtual trial assembly," *Computer-Aided Civil and Infrastructure Engineering*, vol. 36, pp. 453–471, 2020.